Observable Chaos in Switch-Controlled Chua's Circuit

Ali Oksasoglu, Dongsheng Ma, and Qiudong Wang,

This research is partially supported by a grant from NSF.

A. Oksasoglu is with Honeywell, Inc., Tucson, AZ 85737 (email:ali.oksasoglu@honeywell.com).

D. Ma is with the University of Arizona, Department of Electrical and Computer Engineering, Tucson, AZ 85721 (email:ma@ece.arizona.edu).

Q. Wang is with the University of Arizona, Department of Mathematics, Tucson, AZ 85721 (email:dwang@math.arizona.edu).

Observable Chaos in Switch-Controlled Chua's Circuit

Abstract

In this paper, we study the existence of strange attractors in a switch-controlled Chua's circuit. This circuit is obtained from the original Chua's circuit by adding externally controlled switches to it in such a way to modulate the system state variables. This investigation is conducted from the perspective of a recent chaos theory of rank one maps. The externally controlled switches are used for the purposes of realizing the general settings of the theory. Both synchronous and asynchronous switch control schemes providing periodic kicks in various directions are investigated, and their effects on the resulting chaotic attractors are discussed. The results of the numerical simulations presented are in close agreement with the expectations of the theory.

Index Terms

Hopf bifurcation, rank one chaos, strange attractors, nonlinear, Chua's circuit.

I. Introduction

The study of electrical circuits has been a major inspiration for the development of the modern theory of dynamical systems. The existence of asymptotic states of complicated geometrical and dynamical structure was first observed through the studies of the van der Pol system [1], leading to the eventual discovery of strange attractors and the horseshoe maps [2]–[4]. The mathematical analysis and numerical and experimental simulations of electrical systems, such as van der Pol's equation and Duffing's equation, have helped shaping the modern theories of chaos and bifurcations [5]. On the other hand, profound mathematical theories often come back to provide powerful insights, and guide the design of circuit systems of theoretical and practical importance.

Anosov systems and Smale's horseshoes have played central roles for many years in chaos theory. In reality, however, physical and engineering systems are never Anosov, and the horseshoes, the existence of which are often justified by the occurrence of transversal intersections of stable and unstable manifolds, are at the best a small part that is measure theoretically ignorable in a real chaos situation. There have been numerous pictures of chaos generated in the literature. These are often pictures of homoclinic or heteroclinic tangles with geometrical and dynamical structures far more complicated than those of a horseshoe map.

Tangles that are not uniformly hyperbolic are exceedingly complicated and notoriously difficult to analyze. Allowing expanding and contracting behaviors to mix leads to a multitude of possibilities, and in spite of much progress, comprehensive analysis of most non-uniformly hyperbolic systems has remained hopeless to acquire. There is, however, one exception — the analysis of maps of one dimension [6]–[10]. The situation in one dimension is made tractable by the fact that the worst enemy of expansion is the set of critical points. By controlling the orbits starting from the set of critical points, the dynamics on the rest of the phase space can be tamed.

Based on the existing theories of one dimensional maps, Benedicks and Carleson [11] invented a powerful analytical machinery in their study of strongly dissipative Hénon maps, and consequently, opened a door towards a comprehensive understanding of a specific non-Anosov tangle. This analytic machinery is generalized and further developed recently into a theory of rank one attractors by Wang and Young [12], [13]. In [14], [15], this theory is applied to the study of periodically kicked systems of ordinary differential equations of the form,

$$\frac{d\mathbf{u}}{dt} = f(\mathbf{u}) + \varepsilon\Phi(\mathbf{u})P_T(t) \tag{1}$$

where $\mathbf{u} \in \mathbb{R}^m, m \geq 2$, and the second term on the right is a forcing term added to the original system defined by $f(\mathbf{u})$. It was observed that, if the forcing term represents a periodic kick, then the time-T map of (1) in a small neighborhood of a weakly stable limit cycle of the unforced system (i.e., $\varepsilon = 0$) is, in general, a rank one map and the theory developed in [12], [13] applies.

In this paper we introduce a circuit topology as depicted in Fig. 1 to realize the general settings of (1). In this scheme, the state variables are modulated by externally controlled switches. The external control signals are simply periodic pulse trains. When the switches are turned off or at their default positions, the circuit realizes the autonomous part of (1). When they are turned on, specific nonautonomous terms are added as in (1).

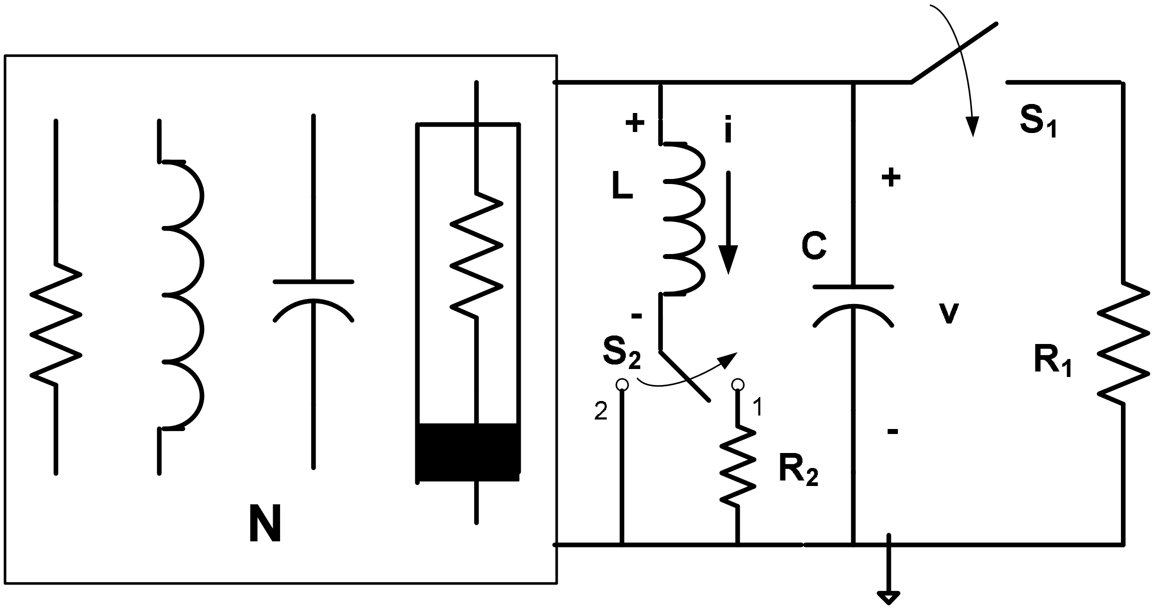

Fig. 1. A switch-controlled network topology

As an example, we employ the scheme of Fig. 1 in the well-known Chua's circuit [16], [17]. The resulting circuit is shown in Fig. 2. Our investigation is based on the theory of rank one attractors and the approach outlined in [18]. That is, we first locate the parameters of Hopf bifurcation for the system under study, then compute the normal form to determine the "twist constant", with which we acquire guidance in finding rank one attractors. From the perspective of the theory of rank one maps, the switches provide a mechanism with which to kick the Hopf limit cycle produced by the original Chua's circuit to generate strange attractors. The existence of rank one attractors in these switch-controlled systems is first proved by using the theories outlined in [18], then confirmed by numerical simulations. The use of multiple switches is to make the choices of $\Phi(\mathbf{u})$ in (1) more flexible. We also employ both synchronous and asynchronous switch control to get rank one attractors of distinctive shapes. In the case of synchronous switch control, identical periodic control pulses are applied to all switches, hence rendering all of them either open or closed at a given time. In the case of asynchronous switch control, periodic control pulses are applied to each of the switch at different times such that at a given time there is at most one activated switch.

There are two main distinctions between the studies of this paper and the rest on the same subject in the literature. First, our study is based on a new chaos theory that is a result of a long and sustained effort from the more analytical and purer side of the dynamical systems community to push the chaos theory beyond the category of uniformly hyperbolic systems and horseshoes. In particular, what is obtained in our numerical simulations is precisely the chaos we prove to exist. Second, we have a recipe-like procedure in creating chaos in circuits of the depiction of Fig. 1, and a systematic way guided by explicit computations in finding them.

This paper is, in a way, a continuation of the studies of rank one attractors in circuit and systems started in [18]. As we will see in Sec. II, the system of differential equations studied in [18] is in fact a specific case obtained from the switch-controlled Chua's circuit shown in Fig. 2.

It is important to note that due to the advances in the semiconductor technology the use of switch-controlled networks can now be seen in almost every area of electrical engineering. We would like to also acknowledge that, in the study of chaotic dynamics, circuits controlled by switches were previously introduced and studied by a group of authors [19]–[26]. These studies, however, are very different in nature from the studies of this paper both in terms of the motivation and the results obtained.

In Sec. II, we derive all the relevant equations for the switch-controlled Chua's circuit. In Sec. III, we present the results of the numerical simulations.

II. Switch-controlled Chua's Circuit and System Equations

In this section we derive the system equations for the switch-controlled Chua's circuit as shown in Fig. 2. Multiple switches are introduced to make the choices of the forcing term in (1) more flexible and to allow asynchronous control of the switches. When the switches S_1 and S_2 are turned off, and S_3 is placed at position 2, the circuit depicted in Fig. 2 is the original Chua's circuit. Note that in the rest of this section we say that the switch S_3 is turned on if it is at position 1, and off if it is at position 2 as shown in Fig. 2.

S_1, S_2 and S_3 are moved by independent periodic control pulses, all of which are periodic functions of t, and of period $T_0 > 0$. Whenever a switch is turned on, it will stay on for a time period of length $p_0 > 0$, which we assume $p_0 << T_0$. Let us denote the times at which the switch S_i is turned on as $s_i + nT_0$. We say that the switches are synchronously controlled if

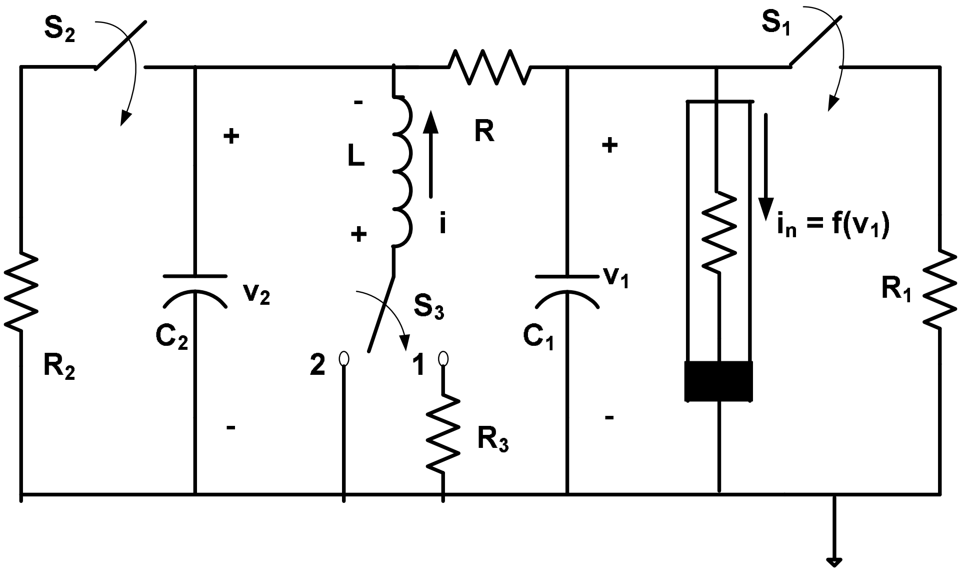

Fig. 2. Switched-controlled Chua's circuit.

$s_1 = s_2 = s_3$. Otherwise the control is asynchronous. In asynchronous control, $s_1,\ s_2,\ s_3$ are so chosen that at most one switch is on at a given time.

Note that the combination of an externally controlled switch and a resistor as depicted in Fig. 1 can be represented as a time-varying resistor whose time-dependent value is given by the periodic pulse train controlling the switch. The equivalent circuit is shown in Fig. 3.

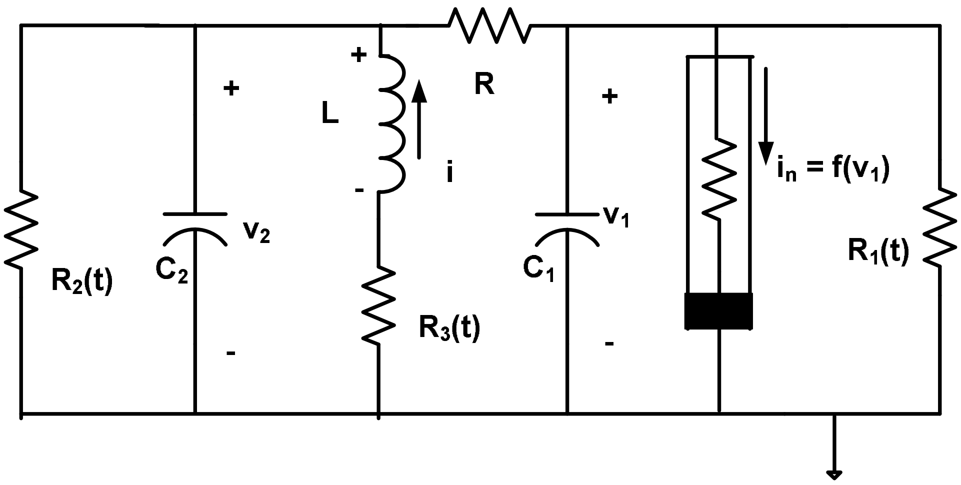

Fig. 3. Equivalent circuit for the switch-controlled Chua's circuit.

A. Synchronous Control

This is the case where all the switches in Fig. 2 are turned on and off at the same time. With p_0 and T_0 being the pulse width and the period, respectively, the switches S_1-S_3 are all on for $nT_0 \leq t < nT_0 + p_0$, and off for $nT_0 + p_0 < t \leq (n+1)T_0$. The governing equations for this circuit are given by

$$\begin{aligned} C_1\frac{dv_1}{dt} =& G(v_2 - v_1) - f(v_1) - G_1 v_1 \\ C_2\frac{dv_2}{dt} =& i + G(v_1 - v_2) - G_2 v_2 \\ L\frac{di}{dt} =& -v_2 - R_3 i \end{aligned} \tag{2}$$

for $nT_0 \leq t < nT_0 + p_0$, and by

$$\begin{aligned} C_1\frac{dv_1}{dt} =& G(v_2 - v_1) - f(v_1) \\ C_2\frac{dv_2}{dt} =& i + G(v_1 - v_2) \\ L\frac{di}{dt} =& -v_2 \end{aligned} \tag{3}$$

for $nT_0 + p_0 \leq t < (n+1)T_0$. Here, $f(\cdot)$ represents the $v - i$ characteristics of the nonlinear resistor in Fig. 2, and is given by

$$f(v_1) = a_1 v_1 + a_3 v_1^3 \tag{4}$$

Putting (2) and (3) together, we obtain

$$\begin{aligned} C_1\frac{dv_1}{dt} =& G(v_2 - v_1) - f(v_1) - G_1 v_1 \sum_{n=0}^{\infty} F_{n,p_0,T_0}(t) \\ C_2\frac{dv_2}{dt} =& i + G(v_1 - v_2) - G_2 v_2 \sum_{n=0}^{\infty} F_{n,p_0,T_0}(t) \\ L\frac{di}{dt} =& -v_2 - R_3 i \sum_{n=0}^{\infty} F_{n,p_0,T_0}(t) \end{aligned} \tag{5}$$

where

$$F_{n,T_0,p_0}(t) = \begin{cases} 1 & nT_0 \leq t < nT_0 + p_0 \\ 0 & elsewhere. \end{cases} \tag{6}$$

By setting

$$x = \frac{v_1}{V_0}, \quad y = \frac{v_2}{V_0}, \quad z = \frac{i}{I_0}, \quad t \to \frac{t}{\omega_n},$$

we obtain the following dimensionless set of equations

$$\begin{aligned}\frac{dx}{dt} &= \alpha[y - h(x)] - \varepsilon_1 x P_{p,T}(t) \\ \frac{dy}{dt} &= \gamma[x - y + \rho z] - \varepsilon_2 y P_{p,T}(t) \\ \frac{dz}{dt} &= -\beta y - \varepsilon_3 z P_{p,T}(t)\end{aligned} \tag{7}$$

where

$$\begin{aligned} P_{p,T} &= \frac{1}{p}\sum_{n=-\infty}^{\infty} F_{n,T,p}, \quad h(x) = b_1 x + b_3 x^3; \\ b_1 &= 1 + \frac{a_1}{G}, \quad b_3 = \frac{a_3 V_0^2}{G}; \\ p &= p_0\omega_n, \quad T = T_0\omega_n; \\ \alpha &= \frac{G}{C_1\omega_n}, \quad \gamma = \frac{G}{C_2\omega_n} = 1.0; \\ \rho &= \frac{R}{R_n}, \quad R_n = \frac{V_0}{I_0}, \quad \beta = \frac{R_n}{L\omega_n}; \\ \varepsilon_1 &= \frac{\alpha R p}{R_1}, \quad \varepsilon_2 = \frac{Rp}{R_2}, \quad \varepsilon_3 = \frac{\beta R_3 p}{R_n}. \end{aligned} \tag{8}$$

B. Asynchronous Control

For simplicity let us only consider the case where we use the same control pulse train for all switches but they are turned on and off at different times. Let us assume that the time the pulse train applied to switch S_i is $s_i + nT_0$, where $s_1 = 0 < s_2 < s_3 < T_0$. Then, the resulting dimensionless set of equations is given by

$$\begin{aligned}\frac{dx}{dt} &= \alpha[y - h(x)] - \varepsilon_1 x P^{(1)}_{p,T}(t) \\ \frac{dy}{dt} &= \gamma[x - y + \rho z] - \varepsilon_2 y P^{(2)}_{p,T}(t) \\ \frac{dz}{dt} &= -\beta y - \varepsilon_3 z P^{(3)}_{p,T}(t)\end{aligned} \tag{9}$$

where, for $i = 1, 2, 3$,

$$
\begin{aligned}
P_{p,T}^{(i)}(t) &= \frac{1}{p}\sum_{n=0}^{\infty} H_{n,T,p,d_i}(t) \\
H_{n,T,p,d_i}(t) &= \begin{cases} 1 & d_i + nT \leq t < d_i + nT + p \\ 0 & elsewhere \end{cases} \\
d_1 = 0 \quad d_2 &= s_2\omega_n, \quad d_3 = s_3\omega_n.
\end{aligned} \tag{10}
$$

The remaining parameters are as given in (8).

Remarks (1) It follows from the derivations of (9) that the actions of the switches S_1-S_3 are independent of each other. Each switch contributes to the nonautonomous term in different directions, i.e, S_1 in x, S_2 in y, and S_3 in z directions. Clearly, we also have the option of keeping one or all three switches turned off. This is equivalent to setting their corresponding forcing term, ε_i, to zero in (9). If, in particular, we keep both S_2 and S_3 in off position forever, we obtain

$$
\begin{aligned}
\frac{dx}{dt} &= \alpha[y - h(x)] - \varepsilon_1 x P_{p,T}^{(1)}(t) \\
\frac{dy}{dt} &= \gamma[x - y + \rho z] \\
\frac{dz}{dt} &= -\beta y.
\end{aligned} \tag{11}
$$

The system of (11) was studied in [18], where the forcing function was simply added to the equation.

(2) The theory developed in [14], [15], which is outlined in [18], only applies to circuits with synchronously controlled switches. There is not yet a theorem which we could apply directly to the asynchronously controlled situation. On the other hand, numerical simulations, as we will see in Sec. III, give many pictures of strange attractors of rich variety both in terms of geometric shape and dynamical structure in the asynchronously controlled circuit. It seems plausible that, under the same guidelines, a rigorous mathematical theorem can be developed in explaining the pictures shown in these simulations. However, such development would be rather long and is clearly out of the scope of this paper. Consequently, the proof on the existence of rank one attractors is restricted to circuits with synchronously controlled switches.

C. *Hopf Bifurcation and the Existence of Rank One Attractors*

The strategy of proving the existence of rank one attractors in systems such as that of (7) (or even (9)) as outlined in [18] is as follows:

(a) First, find a fixed point that is the center of a generic Hopf bifurcation, with a weakly stable periodic solution coming out of the center.

(b) Then, compute the complex normal form for the flow on the central manifold for the Hopf bifurcation located in (a). The ratio of the imaginary and the real parts of the coefficient of the degree three term of this normal form, the so called "twist constant", needs to be sufficiently large for rank one attractors to exist.

(c) Also compute a function $\phi(\theta)$ defined on S^1 through a well-defined process [18], as will be clear later, and check that $\phi(\theta)$ is a Morse function. The rough geometric shape of the rank one attractors is determined by $\phi(\theta)$.

(d) Then the existence of rank one attractors are proved through Propositions 2.1 and 2.2 in [18].

Let us now apply this process to (7).

1) Location of Super-critical Hopf Bifurcation: As we noted earlier, the existing theory only allows us to work with systems with synchronously controlled switches. So here we will work exclusively with Eq. (7), which we rewrite as

$$\frac{d}{dt}\begin{pmatrix} x \\ y \\ z \end{pmatrix} = \begin{pmatrix} -\alpha b_1 & \alpha & 0 \\ 1 & -1 & \rho \\ 0 & -\beta & 0 \end{pmatrix}\begin{pmatrix} x \\ y \\ z \end{pmatrix} + \begin{pmatrix} -b_3\alpha x^3 \\ 0 \\ 0 \end{pmatrix} + \begin{pmatrix} -\varepsilon_1 x \\ -\varepsilon_2 y \\ -\varepsilon_3 z \end{pmatrix} P_{p,T}(t). \tag{12}$$

Let us for the moment fix the values of α, b_1, β and regard ρ as a parameter of bifurcation. Considering the autonomous part of (12), it follows from a straight-forward computation that, at

$$\rho_0 = -\frac{\alpha(b_1-1)(\alpha b_1+1)}{\beta} > 0, \tag{13}$$

the eigenvalues of the linear part of (12) are $\pm i\omega$ and $-(\alpha b_1 + 1)$ where

$$\omega^2 = -\alpha^2 b_1(b_1-1) > 0. \tag{14}$$

Consequently, for a Hopf bifurcation to occur,

$$b_1 \in (0,1). \tag{15}$$

Assuming (15), a generic Hopf bifurcation occur at $(x,y,z)=(0,0,0)$ for the autonomous system obtained by setting $\varepsilon_i=0$ in (12) for $\rho=\rho_0$. As ρ changes passing ρ_0, the origin becomes unstable, but a weakly stable periodic solution comes out of it. From this point on, all computations are performed at $\rho=\rho_0$.

To convert the linear part of (12) into the standard Jordan form we let

$$\begin{pmatrix} x \\ y \\ z \end{pmatrix} = \mathbf{P}\begin{pmatrix} \xi \\ \eta \\ \zeta \end{pmatrix} = \begin{pmatrix} 1 & \frac{\omega}{\alpha b_1} & -\alpha \\ 1 & 0 & 1 \\ 0 & -\frac{\beta}{\omega} & \frac{\beta}{\alpha b_1+1} \end{pmatrix}\begin{pmatrix} \xi \\ \eta \\ \zeta \end{pmatrix} \tag{16}$$

with

$$\mathbf{P}^{-1} = \frac{\omega(\alpha b_1+1)}{\beta[\alpha b_1(\alpha+2)+1]}\begin{pmatrix} \frac{\beta}{\omega} & \frac{\alpha\beta b_1(\alpha+1)}{\omega(\alpha b_1+1)} & \frac{\omega}{\alpha b_1} \\ -\frac{\beta}{\alpha b_1+1} & \frac{\beta}{\alpha b_1+1} & -(\alpha+1) \\ -\frac{\beta}{\omega} & \frac{\beta}{\omega} & -\frac{\omega}{\alpha b_1} \end{pmatrix}. \tag{17}$$

In terms of the new variables ξ,η and ζ, (12) becomes

$$\begin{aligned} \frac{d\xi}{dt} &= \omega\eta - c_0(\xi + \frac{\omega}{\alpha b_1}\eta - \alpha\zeta)^3 + \Phi_\xi P_{p,T}(t) \\ \frac{d\eta}{dt} &= -\omega\xi + c_0\frac{\omega}{1+\alpha b_1}(\xi + \frac{\omega}{\alpha b_1}\eta - \alpha\zeta)^3 + \Phi_\eta P_{p,T}(t) \\ \frac{d\zeta}{dt} &= -(\alpha b_1+1)\zeta + c_0(\xi + \frac{\omega}{\alpha b_1}\eta - \alpha\zeta)^3 + \Phi_\zeta P_{p,T}(t) \end{aligned} \tag{18}$$

where

$$c_0 = \frac{\alpha b_3(\alpha b_1+1)}{\alpha^2 b_1 + 2\alpha b_1 + 1} \tag{19}$$

and

$$\begin{aligned} \Phi_\xi &= -\frac{\alpha b_1+1}{\alpha^2 b_1+2\alpha b_1+1}\left\{\left(\varepsilon_1 + \frac{b_1(\alpha+1)}{\alpha b_1+1}\varepsilon_2\right)\xi + \frac{\omega}{\alpha b_1}(\varepsilon_1-\varepsilon_3)\eta \right. \\ &\quad \left. + \left(-\alpha\varepsilon_1 + \frac{\alpha b_1(\alpha+1)}{\alpha b_1+1}\varepsilon_2 + \frac{\alpha(1-b_1)}{\alpha b_1+1}\varepsilon_3\right)\zeta\right\} \\ \Phi_\eta &= -\frac{\omega(\alpha b_1+1)}{\alpha^2 b_1+2\alpha b_1+1}\left\{\frac{1}{\alpha b_1+1}(-\varepsilon_1+\varepsilon_2)\xi - \frac{1}{\omega}\left(\frac{\alpha(1-b_1)}{\alpha b_1+1}\varepsilon_1 - (\alpha+1)\varepsilon_3\right)\eta \right. \\ &\quad \left. + \left(\frac{\alpha}{\alpha b_1+1}\varepsilon_1 + \frac{1}{\alpha b_1+1}\varepsilon_2 - \frac{\alpha+1}{\alpha b_1+1}\varepsilon_3\right)\zeta\right\} \\ \Phi_\zeta &= -\frac{(\alpha b_1+1)}{\alpha^2 b_1+2\alpha b_1+1}\left\{(\varepsilon_1-\varepsilon_2)\xi + \frac{\omega}{\alpha b_1}(\varepsilon_1-\varepsilon_3)\eta + \left(-\alpha\varepsilon_1+\varepsilon_2-\frac{\alpha(1-b_1)}{\alpha b_1+1}\varepsilon_3\right)\zeta\right\}. \end{aligned} \tag{20}$$

2) Normal Form and the Twist Constant: We now compute the central manifold and the normal form. Let

$$\zeta = h_2(\xi, \eta) + h_3(\xi, \eta) + \cdots \tag{21}$$

be the central manifold at $\xi = \eta = \zeta = 0$ where h_i are the terms of degree i. Because the starting non-linear term in (18) is of degree three, we have

$$h_2(\xi, \eta) = 0. \tag{22}$$

So in computing the normal form we can practically regard the central manifold as $\zeta = 0$. If we define $z = \xi + i\eta$, then

$$\xi = \frac{1}{2}(z + \bar{z}), \qquad \eta = \frac{1}{2i}(z - \bar{z}). \tag{23}$$

We set $\zeta = 0$ in (18), to obtain

$$\frac{dz}{dt} = -\omega i z + \frac{1}{8}c_0(-1 + i\frac{\omega}{1 + \alpha b_1})(z + \bar{z} - \frac{\omega}{\alpha b_1}(z - \bar{z})i)^3. \tag{24}$$

Note that k_1 is the coefficient in front of $z^2\bar{z}$. Thus we have

$$k_1 = c_1(1 + 2\alpha b_1 - \alpha - \frac{\omega}{\alpha b_1}(1 + 2\alpha b_1)i) \tag{25}$$

where

$$c_1 = \frac{-3c_0}{8b_1(1 + \alpha b_1)}. \tag{26}$$

Hence the twist constant

$$\tau := \left|\frac{Im(k_1)}{Re(k_1)}\right| = \left|\frac{\omega(1 + 2\alpha b_1)}{\alpha b_1(1 + \alpha b_1 - \alpha)}\right|. \tag{27}$$

3) The function $\phi(\theta)$ and the Existence of Rank One Attractors: The function $\phi(\theta)$ is computed by first setting $\zeta = 0$ in Φ_ξ and Φ_η to obtain

$$\begin{aligned} \Phi_\xi &= -\frac{\alpha b_1 + 1}{\alpha^2 b_1 + 2\alpha b_1 + 1}\left\{(\varepsilon_1 + \frac{b_1(\alpha + 1)}{\omega b_1 + 1}\varepsilon_2)\xi + \frac{\omega}{\alpha b_1}(\varepsilon_1 - \varepsilon_3)\eta\right\} \\ \Phi_\eta &= -\frac{\omega(\alpha b_1 + 1)}{\alpha^2 b_1 + 2\alpha b_1 + 1}\left\{\frac{1}{\alpha b_1 + 1}(-\varepsilon_1 + \varepsilon_2)\xi - \frac{1}{\omega}\left(\frac{\alpha(1 - b_1)}{\alpha b_1 + 1}\varepsilon_1 - (\alpha + 1)\varepsilon_3\right)\eta\right\}. \end{aligned} \tag{28}$$

We then set $\xi = \cos\theta, \eta = \sin\theta$ and

$$\begin{aligned}\phi(\theta) &= \frac{1}{\varepsilon_1}[\cos\theta\Phi_\xi + \sin\theta\Phi_\eta] \\ &= c_2\left\{\left(1 + \frac{b_1(\alpha+1)}{\omega b_1 + 1}\frac{\varepsilon_2}{\varepsilon_1}\right)\cos^2\theta + \frac{\omega}{\alpha b_1(\alpha b_1+1)}(1 + \alpha b_1\frac{\varepsilon_2}{\varepsilon_1} - (\alpha b_1 + 1)\frac{\varepsilon_3}{\varepsilon_1})\cos\theta\sin\theta \right.\\ &\quad \left. -\frac{1}{\omega}\left(\frac{\alpha(b_1-1)}{\alpha b_1+1} - (\alpha+1)\frac{\varepsilon_3}{\varepsilon_1}\right)\sin^2\theta\right\}\end{aligned} \tag{29}$$

where

$$c_2 = -\frac{\alpha b_1 + 1}{\alpha^2 b_1 + 2\alpha b_1 + 1}.$$

Assuming that $\phi(\theta)$ in the above is a Morse function, i.e., all critical point of $\phi(\theta)$ are non-degenerate, then the existence of rank one attractors for (18) follows from Proposition 2.1 and 2.2 in [18]. Note that, in general, $\phi(\theta)$ in the above is a Morse function unless all three coefficients of $\cos^2\theta$, $\cos\theta\sin\theta$ and $\sin^2\theta$ are zero.

III. Numerical Simulations

A. *Observable Chaos: A Theoretical Discussion*

To explain the main difference between the chaos we proved to exist in Sec. II and the ones obtained previously in the literature, let us look more closely on the concept of chaos and the mathematical theory so far used to justify their existence. It has been universally agreed that chaos is a dynamical phenomenon characterized by sensitive dependence of orbits on initial conditions and the unpredictability of destinations of any given individual orbit. These terms are however only rough descriptions, good enough perhaps for demonstration but not precise enough to be taken as a base on which to build a rigorous theory. The efforts to develop a chaos theory with mathematical precision have led to powerful innovations, and consequently to the development of the modern theory of dynamical systems.

Along the way of this magnificent development there is always the issue of finding chaos in concrete systems. For someone who is more mathematically oriented this is an issue of proving **rigorously** that chaos exists in a given system, and for people of more practical concern this is an issue of finding chaos in their own systems through some sort of simulations. When studying a concrete system, the ideal scenario would be to have both, i.e., rigorous proof of existence and demonstration by simulation. The standard for the latter is more or less uniform because chaos is easy to recognize in pictures. The former, however, is where people diverge. The precise meaning of the word "chaos" differs from author to author.

Despite all variations, however, there have been one thing that is dictating in the studies of chaos in *concrete* systems, namely, the horseshoe map.[1] There has been a steadily growing tendency to take the occurrence of horseshoe maps as a sufficient condition for the existence of chaos. Smale's finding that homoclinic tangles imply horseshoes has been so influential that many people identify the existence of chaos with the existence of homoclinic tangles. This identification is also convenient in practice since transversal intersections of stable and unstable manifolds are readily checked, and are by definition robust. The robustness is, in particular, very comforting: transversal intersections, if exist, will persist under small perturbations. Therefore, not only chaos is shown to exist, but also it will show up in simulations.

Is it necessarily the case that the existence of homoclinic tangles in a given system implies the existence of chaos as shown in the pictures of various simulations? The answer is, unfortunately, **negative**. As an example let us look at Figs. 17 and 18 in Sec. III-C. It is clear that Fig. 17 is a picture of chaos and Fig. 18 is not. However, we can prove rigorously without much trouble that both maps in the part of the phase space depicted in Figs. 17 and 18 do contain homoclinic tangles. This now sounds like a paradox: do we have homoclinic tangles in the system depicted in Fig. 18? Yes! Then, why does it not show up in simulations?

The answer lies in the fact that, in general, homoclinic tangles contain more than horseshoes. It is entirely possible (as a matter of fact, typical), for instance, for a tangle to contain a sink, which represents non-chaotic behavior. A sink, if exists, possesses a basin that is open. Not the same for horseshoes: they are in general Cantor sets of zero measure and so is the set they attract. Fig. 18 represents a case in which sinks in homoclinic tangles attract *almost every point* of the basin. Since simulations could never hit a set of measure zero, there is no chaos showing up.

To the best of our knowledge, all proofs of chaos in circuits in previous literature are essentially proofs of the existence of homoclinic tangles and horseshoes. However, homoclinic tangles alone are not sufficient in justifying the pictures of chaos shown through simulations. These are pictures of homoclinic tangles without sinks. To distinguish tangles with sinks from those without is a

[1]Here we should perhaps exclude the vast subject of billiards.

mathematical question of notorious difficulty, and it is for this matter that the theory of rank one maps is developed. This new mathematical theory is the first, and the only one so far, that enables us to match precisely what is rigorously proved with what occurs in simulations of electronic circuits.

B. *Observable Chaos: Simulation Results*

In this subsection, we present pictures of chaotic attractors obtained by numerical simulations. As we will see in the next two subsections, these are not the only kind we encounter. The parameters $\alpha = 2, \beta = 2, b_1 = 0.242, b_3 = 1, \rho = \rho_0 - 0.005 = 1.119872$ are fixed throughout. With the choices of these parameter values we are close to a Hopf bifurcation (appears at $\rho_0 = 1.124872$) with a relatively large twist constant. When all three switches are in action we set $\varepsilon_1 = 0.52,\ \varepsilon_2 = 0.32$, and $\varepsilon_3 = 0.26$. Each switch is either included in the simulation with these assigned ε_i values or disabled by setting its respective ε_i value to zero. For instance, to remove S_3 from the circuit we set $\varepsilon_3 = 0$ while keeping $\varepsilon_1 = 0.52,\ \varepsilon_2 = 0.32$. In all cases, we let p, the length of time during which the switches are on, be fixed at $p = 0.5$. For the synchronous control, we set $s_1 = s_2 = s_3 = 0$, and for the asynchronous control, $s_1 = 0, s_2 = 50, s_3 = 100$. The guidelines in our choice of these parameters are as follows:

(1) We must be close to a point of Hopf bifurcation with a large twist constant.

(2) After a switch is turned off, there should be a relatively long relaxation period during which all switches are kept off.

(3) ε_i are reasonably small so that the orbit is not kicked forever out of the neighborhood of the Hopf bifurcation. On the other hand, they should be reasonably large to make it possible to obtain pictures of rank one attractors.

The selection of parameter values above is made with these considerations in mind. Otherwise, our choice of parameters is quite arbitrary. The qualitative aspects of the pictures we present would not alter if a different set of parameters were used. Note that compared to the simulations conducted in [18] ($\varepsilon \approx 0.15$), the current values of ε_i are much larger. This is designed to make pictures of chaos easier to obtain.

Our simulations are performed using the fourth-order Runge-Kutta routine starting at $t_0 = 0$. For all pictures presented, one discrete orbit started near the attractor for the time-T map is presented. With the values of parameters fixed as specified above, the things left available for us to vary are (i) the period T, (ii) the number of switches to include, and (iii) synchronous or asynchronous switch control scheme.

The limit cycle obtained by setting $\varepsilon_1 = \varepsilon_2 = \varepsilon_3 = 0$ is shown in Fig. 4. Figures 5-8 are the first set of pictures of chaotic attractors we choose to present. For Fig. 5 we remove S_2 and S_3 by letting $\varepsilon_2 = \varepsilon_3 = 0$, and set $T = 78.5$. In Figs. 6 and 7 we keep S_1 and S_2 but set $\varepsilon_3 = 0$ to remove S_3. For Fig. 6, we let $s_1 = s_2 = 0$ so the switches S_1 and S_2 are synchronously controlled. For Fig. 7, $s_1 = 0$, $s_2 = 50$, so S_1 and S_2 are asynchronously controlled. For Fig. 6, $T = 144.5$ and for Fig. 7, $T = 160.5$. Fig. 8 is a simulation of an asynchronously controlled circuit in which all three switches are in action, for which $T = 200$. With more switches in action and asynchronous control, the complexity in the rough geometric shape and dynamical structure of the chaotic attractors apparently increase, as shown in these pictures.

The length of the relaxation period, that is the time from the last switch is turned on to the beginning of the next period, is relatively short for Figs. 5-8. The rank one character in these pictures are not clearly shown, but the initial deformation caused by the forcing terms are exaggerated enough by a large twist constant so that chaotic attractors are created. In Figs. 9-12 we make T larger. It is clear that the arms in these pictures are stretched longer, and they wrap around. Again, the complexity of the geometrical shape and the dynamics increases as we move from the case of one switch (Fig. 9) to two switches (Figs. 10 and 11), and to all switches asynchronously controlled (Fig. 12).

Our next set, Figs. 13 and 15, are those of real rank one attractors proved to exists in Sec. II. Fig. 13 corresponds to the systems of Figs. 5 and 9, and Fig. 15 to the systems of Figs. 8 and 12. (We skip the pictures for the cases in between to avoid redundancy, they do exist nevertheless). With very long relaxation periods, the attractors are pressed down in the radial direction, with the look of a simple curve. These are, however, pictures of chaotic attractors of extreme complexity. For these strange attractors, the complexity displayed in Figs. 5-12 do not disappear: they are simply compressed so thin that they do not show up in Figs. 13 and 15. The locally magnified structures of Figs. 13 and 15 are shown in Figs. 14 and 16, respectively.

C. Tangles with Dominating Sinks

Chaos shown in Figs. 5-16 are pictures of homoclinic tangles **without sinks**. To distinguish the chaos of this kind from those defined previously in the literature based only on the existence of homoclinic tangles, we will from this point on call them **observable chaos** (those seen in simulations). This implies that there is "chaos" (tangles) that is not observable. One conclusion coming out of the theory of rank one maps is that, unlike uniformly hyperbolic systems, *observable chaos* is not robust under small perturbations of parameters. Take F_T, the time-T maps of Eq. (9), for an example. Let us fix the values of all parameters other than T, and assume that F_{T_1} admits an observable chaos. To the question that if there exists a sufficiently short interval I around T_1 such that F_T admits an observable chaos for all $T \in I$, the answer is definitely negative. In other words, the set of T such that F_T admits an observable chaos is nowhere dense (has no open interior). Let us emphasize that, this lack of robustness of observable chaos is not an exceptional phenomenon, but a matter of life. Observable chaos in systems that are not uniformly hyperbolic has no persistency under small perturbations of parameters. These include all real physical and engineering systems. No topological persistency, no structural stability exist for "observable chaos".

To demonstrate this sensitive dependency on parameters by numerical simulations, let us again set $\alpha = 2, \beta = 2, b_1 = 0.242, b_3 = 1, \rho = 1.119872$ and $s_1 = 0$, $s_2 = 50$ $s_3 = 100$, all the same as before. We, however, make the values of ε_i smaller: $\varepsilon_1 = 0.25$, $\varepsilon_2 = 0.15$ and $\varepsilon_3 = 0.10$. Our reason for such modifications of ε_i will become clear momentarily. Figs. 17 and 18 are both obtained by setting $\varepsilon_2 = \varepsilon_3 = 0$, but Fig. 17 is for $T = 290.5$, Fig. 20 is for $T = 291.0$. A difference of 0.5 in T changes the time-T map from that of a chaos to that of a sink. Figs. 19 and 20 are other examples with all three switches in asynchronous action. $T = 294.0$ for Fig. 19 and $T = 293.5$ for Fig. 20. Such sensitive dependence of dynamical patterns on T is rather typical, and is encountered all the time in simulations.

Let us note again that, homoclinic tangles, therefore horseshoes exist for the maps of both Figs. 18 and 20, and the reason we do not see chaos in these simulations is because these tangles contain also sinks that attract almost every point in the basin. Numerical simulations cannot possibly hit these horseshoes because they only attract a set of negligible measure.

D. Robustness of Strange Attractor

The lack of stability of observable chaos discussed in Sec III-C is obviously a concern of practical consequences. In general, equations from theory are only approximations of real physical or engineering systems, and the viability of non-persistent phenomenon in mathematical model is potentially a serious problem in practical applications. A solution on this issue of robustness concerning observable chaos (with some level of mathematical subtlety) is obtained in the theory of rank one maps.

The solution is as follows: since the set of parameters admitting observable chaos is nowhere dense, it is not possible for us to tell if a specific system of a given parameter value contains observable chaos or not. However, for certain intervals of parameters, we know that the measure of the set of parameters that give rise to observable chaos is **positive**, implying that, by randomly experimenting on this interval, one hits observable chaos with positive probability. The measure of this set of parameters could be small or big depending on the location of parameters, but we know how to make it big. For the time-T map of (9), larger twist constants and ε values are for it, and smaller values are against it. As a matter of fact, for the parameters used in Sec. III-B, the relative measure for observable chaos is close to one so we hit pictures of chaos almost all the time in the simulations. As we lower the values of ε_i, the measure of the set of parameters for observable chaos becomes smaller. For instance, our chance of hitting chaos in our simulations becomes half and half with the values used in Sec. III-C. If we lower the values of ε_i further (or move to a place where the twist constant is smaller), the chance of hitting chaos in the simulations gets slimmer. For instance, by setting $\varepsilon_1 = 0.15$, $\varepsilon_2 = \varepsilon_3 = 0$, and keeping other parameters the same as those of Figs. 10-14, the chance of hitting chaos is reduced to one out of every thirty tries. With the parameter values used in Sec. III-B, it is very hard to hit pictures that are not chaotic. This is why we use smaller ε_i in Sec. III-C. It is in this probabilistic sense that the robustness of observable chaos is maintained, as predicted by the theory and confirmed by the simulations.

IV. Conclusion

The purpose of this paper was two-fold. The first was to find real applications in circuits or systems for a new theory developed only recently. The second purpose was to introduce this new theory to the part of the engineering sciences community that is interested in chaos theory and its applications. As stated before, this new chaos theory is a result of a long and sustained effort from the more analytical and purer side of the dynamical systems community to push the chaos theory beyond the category of uniformly hyperbolic systems and horseshoes. It is, both in terms of its mathematical subtlety and its ability in matching results of proofs and simulations, a substantial improvement over the previous studies based on the existence of homoclinic tangles and horseshoes.

The electronic system studied in this paper is a switch-controlled Chua's circuit. The switches are used to realize the type of the forcing term needed in generating chaos. A recipe-like procedure for creating chaos, and a systematic way of finding it through explicit computations are laid out in details. The existence of *observable chaos* is obtained both theoretically and numerically under the guideline of the theory. We found that, the use of multiple switches under the asynchronous control scheme tends to increase the complexity of chaos both in terms of rough geometrical shapes and dynamical complexity. The issues covered in this paper include the differences concerning the existence of *observable chaos* and that of homoclinic tangles, the sensitive dependence of dynamical structure on parameters, and the robustness of observable chaos. Both, theoretical proofs and results of simulations are presented.

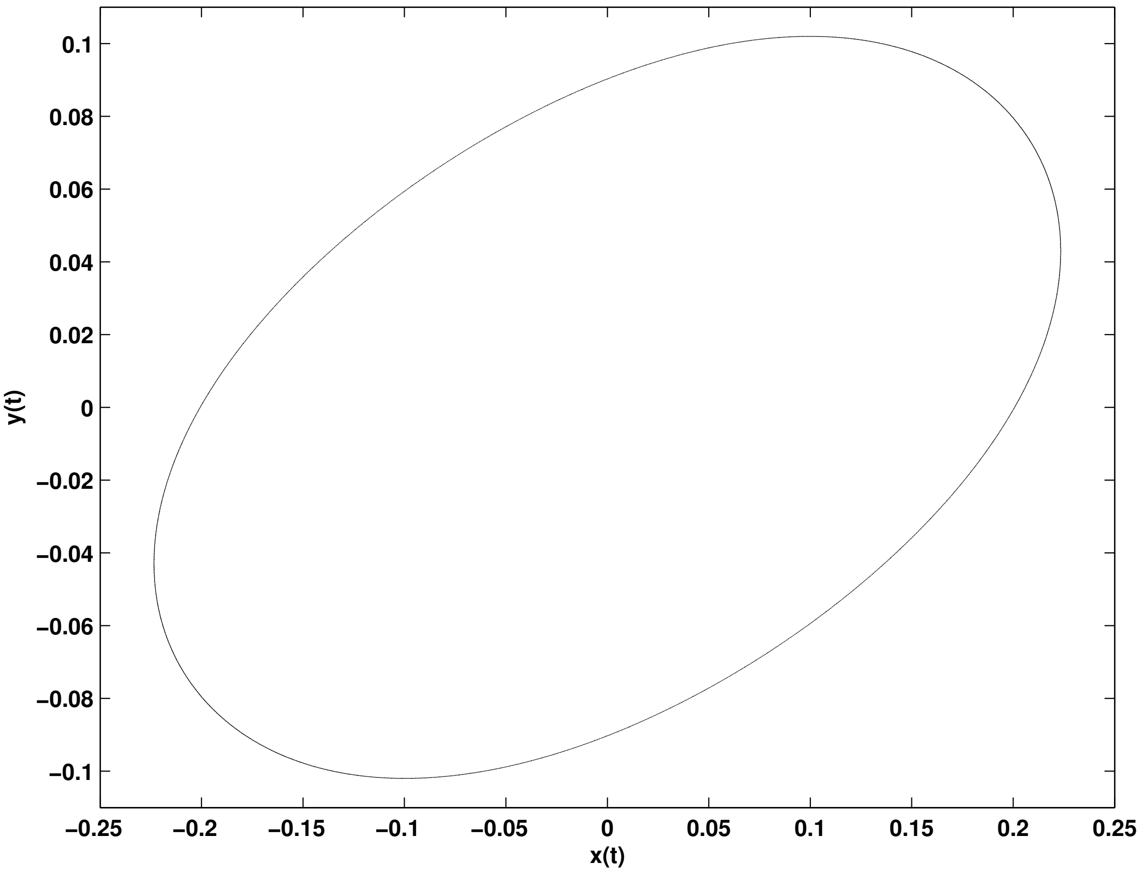

Fig. 4. A Hopf limit cycle ($\varepsilon_1 = \varepsilon_2 = \varepsilon_3 = 0$).

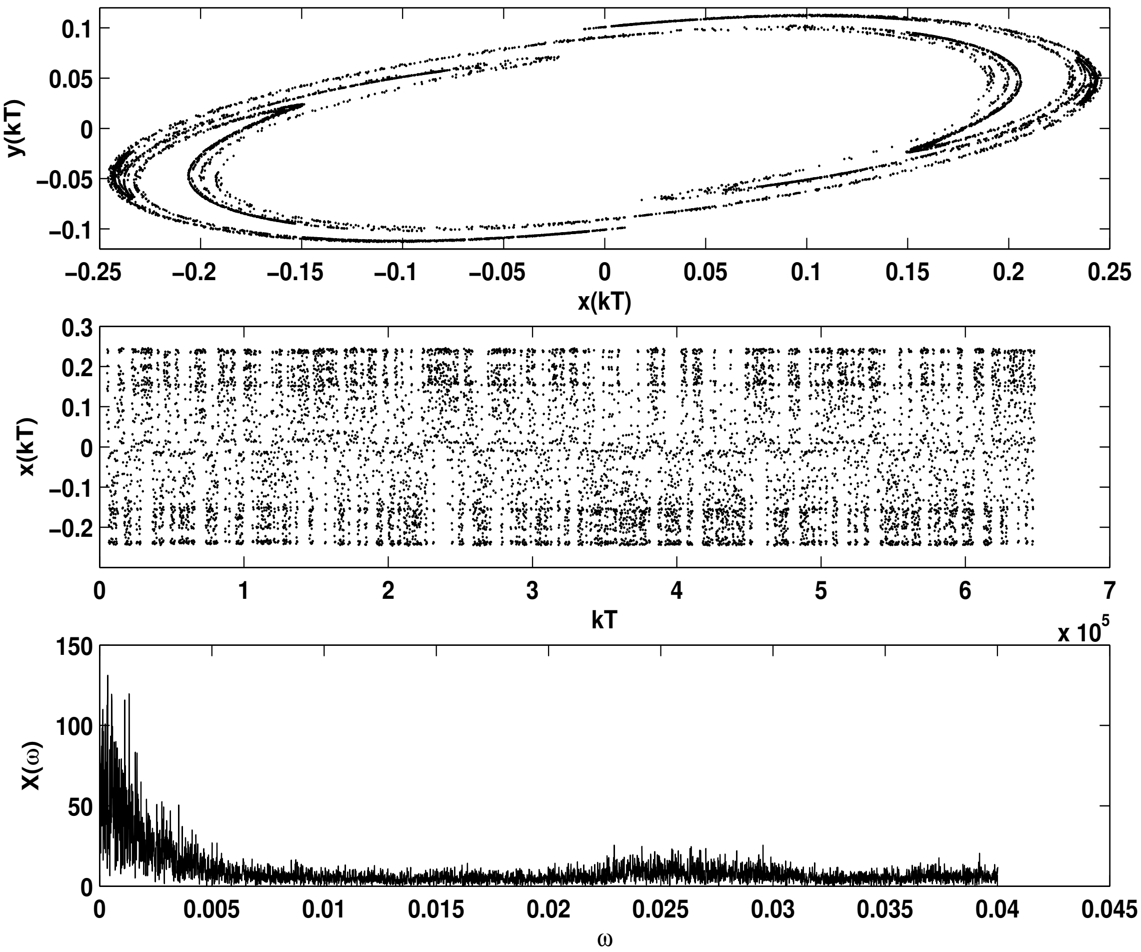

Fig. 5. Strange attractor, $T = 78.5, \varepsilon_1 = 0.52, \varepsilon_2 = \varepsilon_3 = 0$. Time-T map projected onto $x - y$ plane (top), $x(kT)$ versus kT (middle), frequency spectrum of $x(kT)$ (bottom).

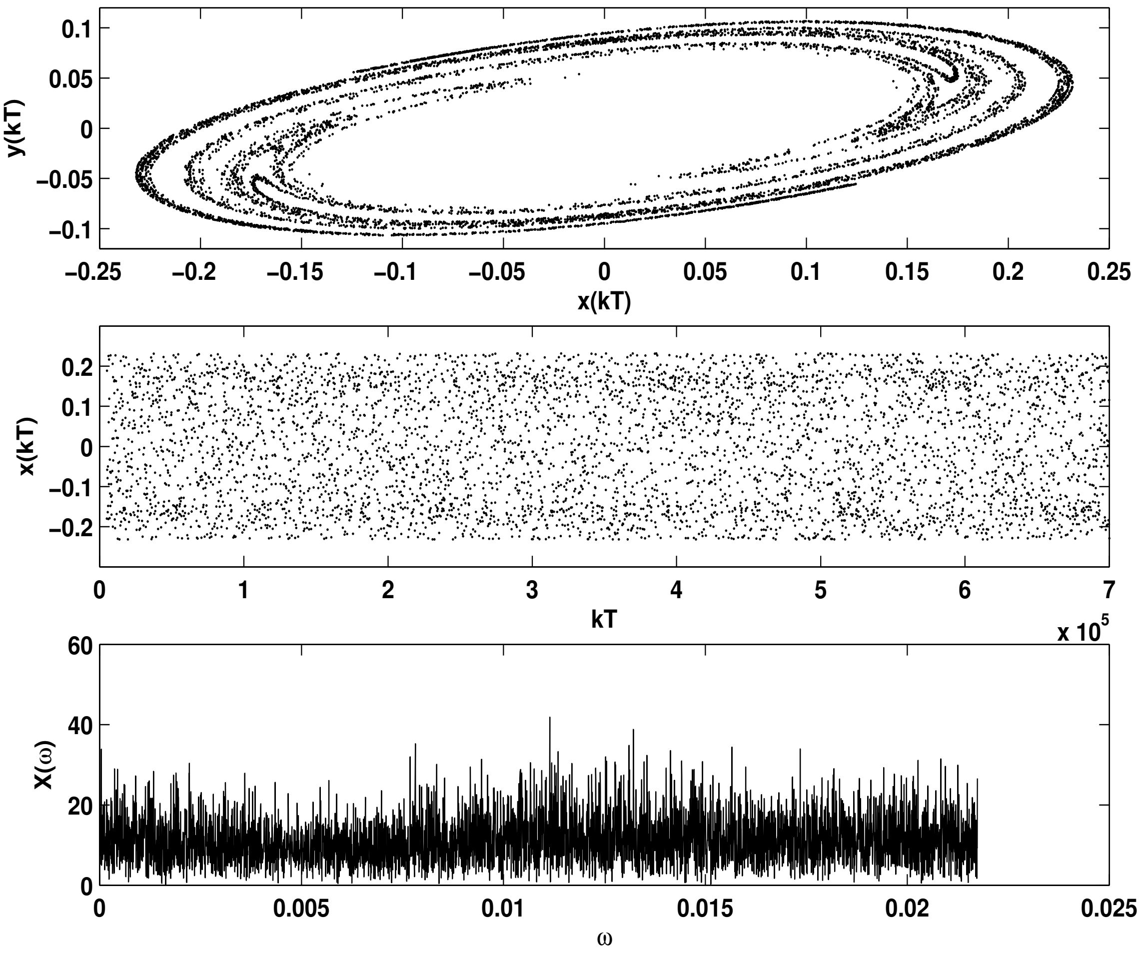

Fig. 6. Strange attractor (Synchronous case), $T = 144.5, \varepsilon_1 = 0.52, \varepsilon_2 = 0.32, \varepsilon_3 = 0$. Time-T map projected onto $x - y$ plane (top), $x(kT)$ versus kT (middle), frequency spectrum of $x(kT)$ (bottom).

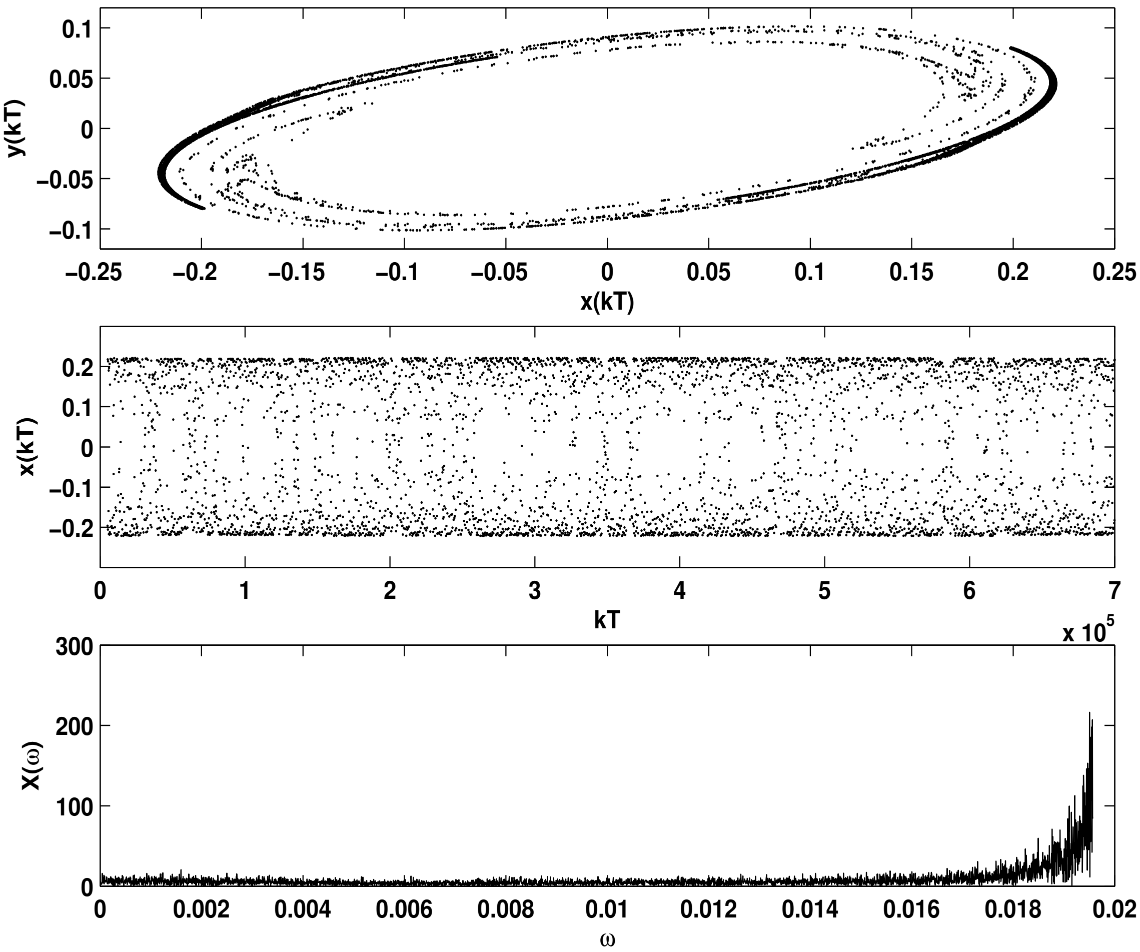

Fig. 7. Strange attractor (Asynchronous case), $T = 160.5, \varepsilon_1 = 0.52, \varepsilon_2 = 0.32, \varepsilon_3 = 0$. Time-T map projected onto $x - y$ plane (top), $x(kT)$ versus kT (middle), frequency spectrum of $x(kT)$ (bottom).

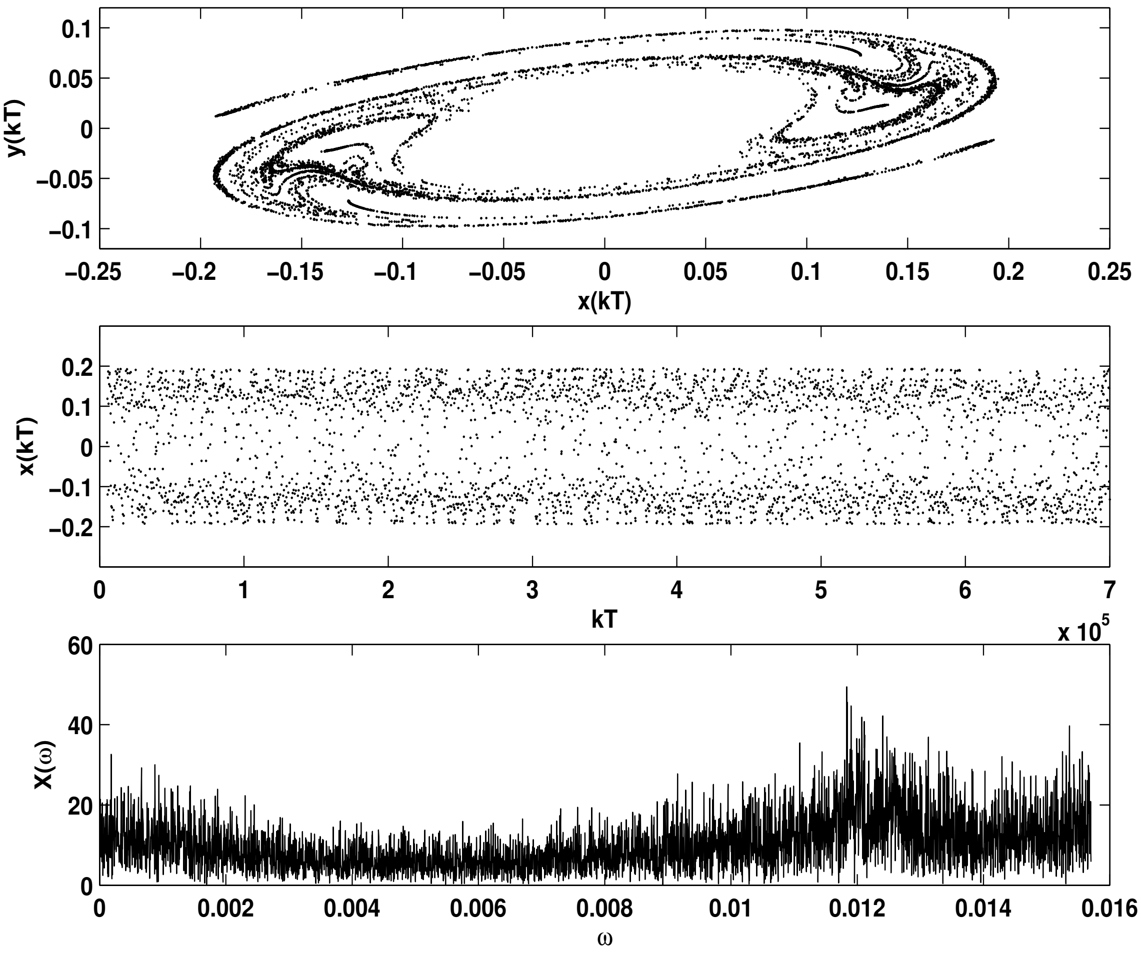

Fig. 8. Strange attractor (Asynchronous case), $T = 200, \varepsilon_1 = 0.52, \varepsilon_2 = 0.32, \varepsilon_3 = 0.26$. Time-T map projected onto $x - y$ plane (top), $x(kT)$ versus kT (middle), frequency spectrum of $x(kT)$ (bottom).

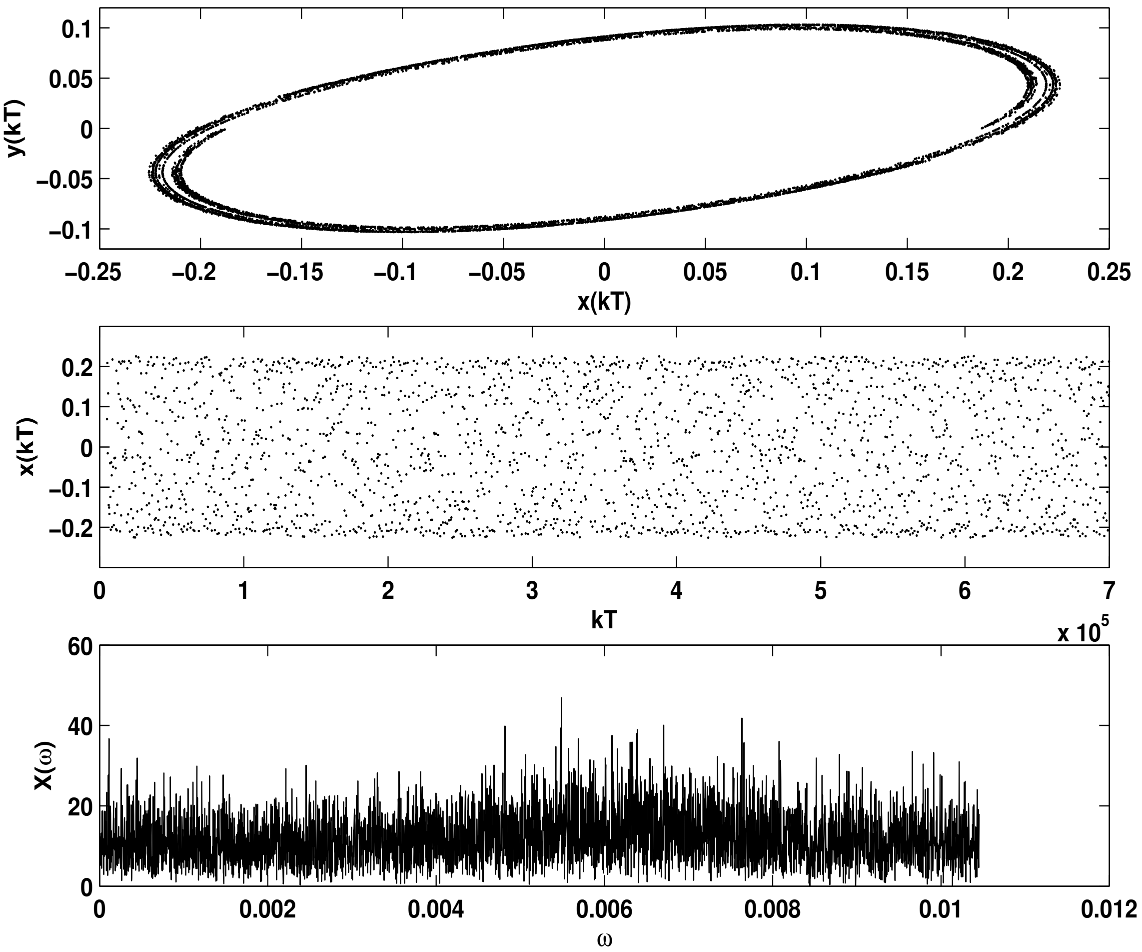

Fig. 9. Strange attractor, $T = 300.5, \varepsilon_1 = 0.52, \varepsilon_2 = \varepsilon_3 = 0$. Time-T map projected onto $x - y$ plane (top), $x(kT)$ versus kT (middle), frequency spectrum of $x(kT)$ (bottom).

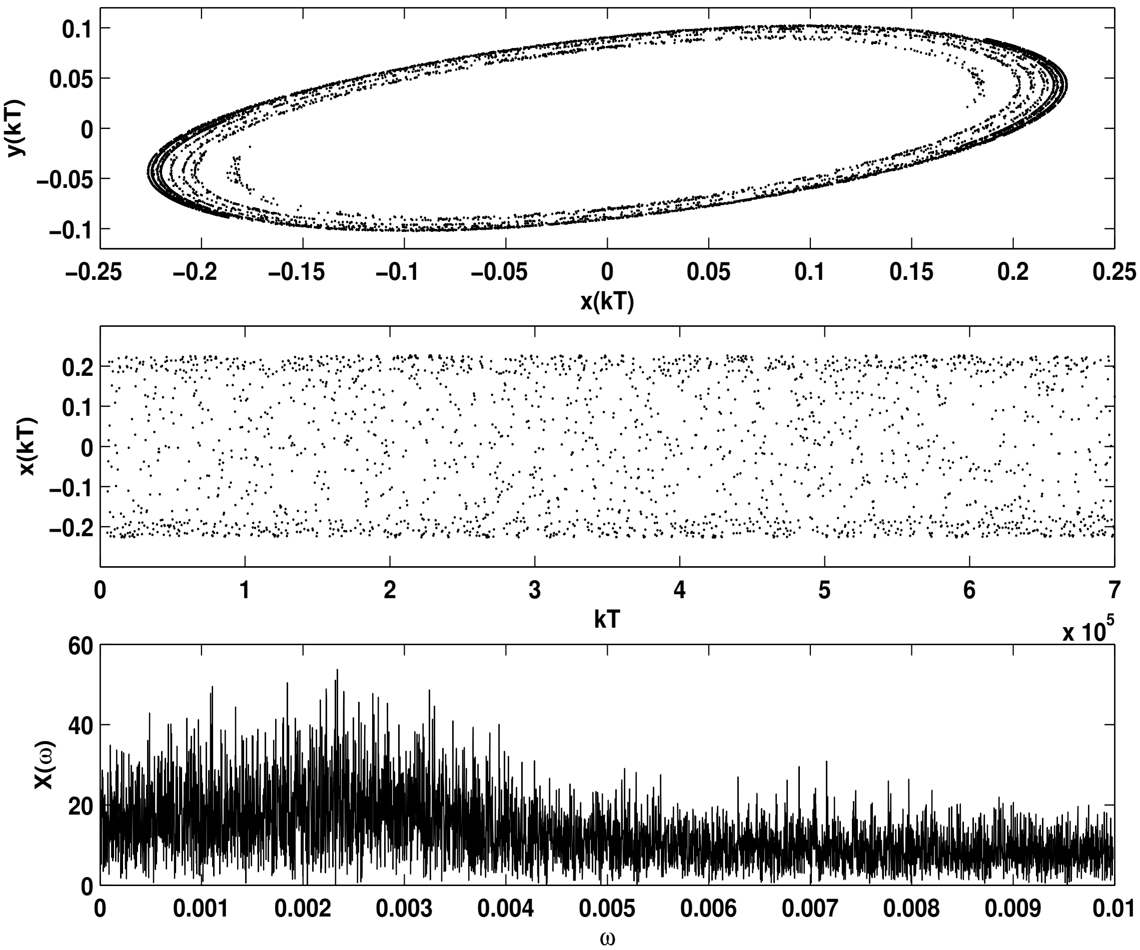

Fig. 10. Strange attractor (Synchronous case), $T = 314.5, \varepsilon_1 = 0.52, \varepsilon_2 = 0.32, \varepsilon_3 = 0$. Time-T map projected onto $x - y$ plane (top), $x(kT)$ versus kT (middle), frequency spectrum of $x(kT)$ (bottom).

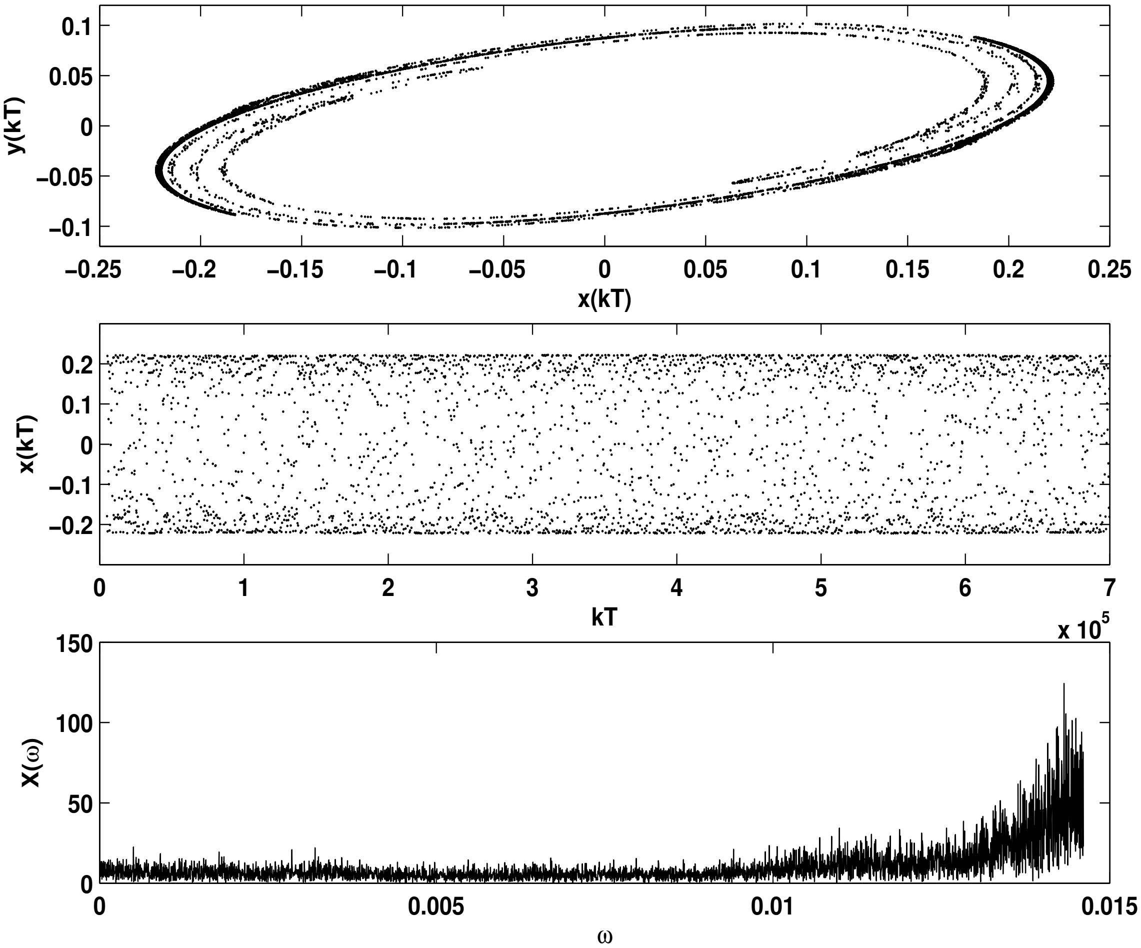

Fig. 11. Strange attractor (Asynchronous case), $T = 215, \varepsilon_1 = 0.52, \varepsilon_2 = 0.32, \varepsilon_3 = 0$. Time-T map projected onto $x - y$ plane (top), $x(kT)$ versus kT (middle), frequency spectrum of $x(kT)$ (bottom).

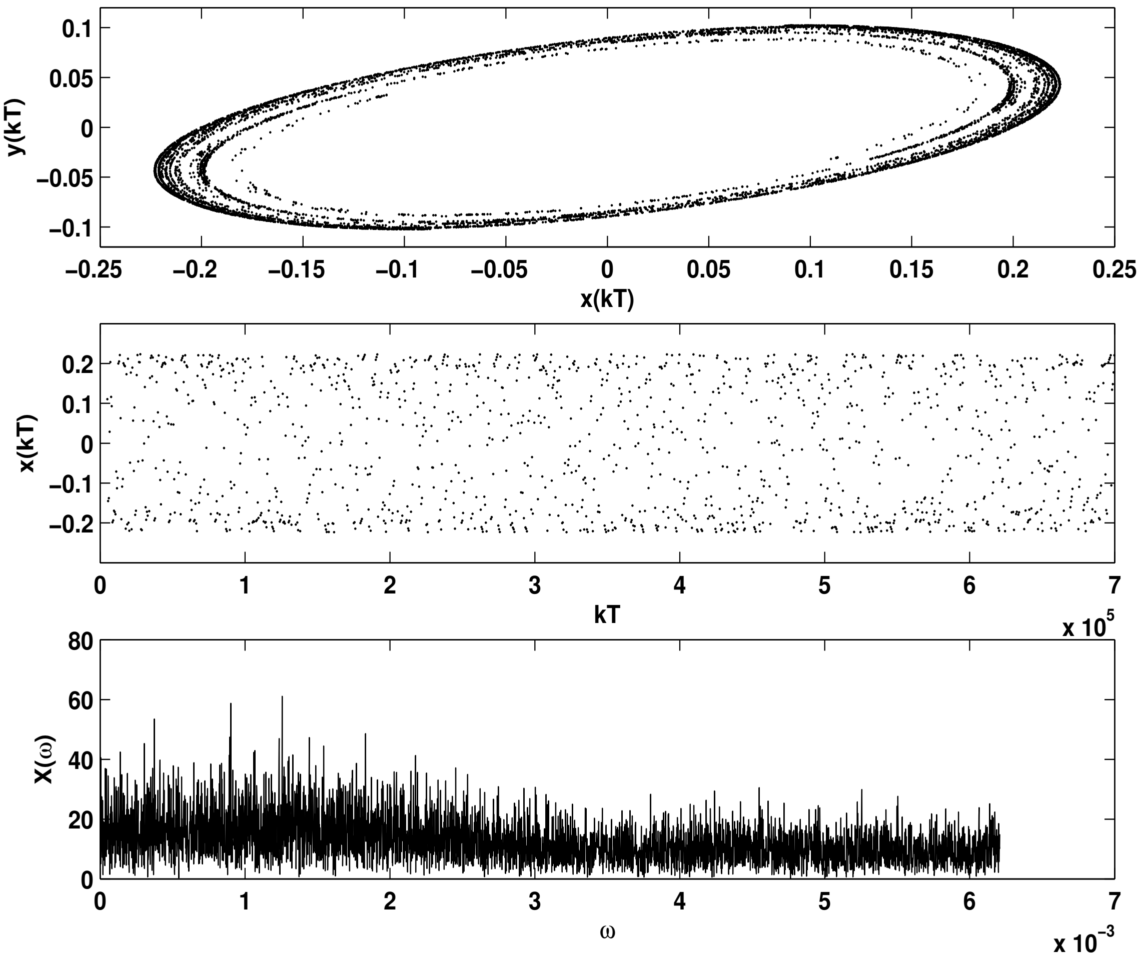

Fig. 12. Strange attractor (Asynchronous case), $T = 506, \varepsilon_1 = 0.52, \varepsilon_2 = 0.32, \varepsilon_3 = 0.26$. Time-T map projected onto $x - y$ plane (top), $x(kT)$ versus kT (middle), frequency spectrum of $x(kT)$ (bottom).

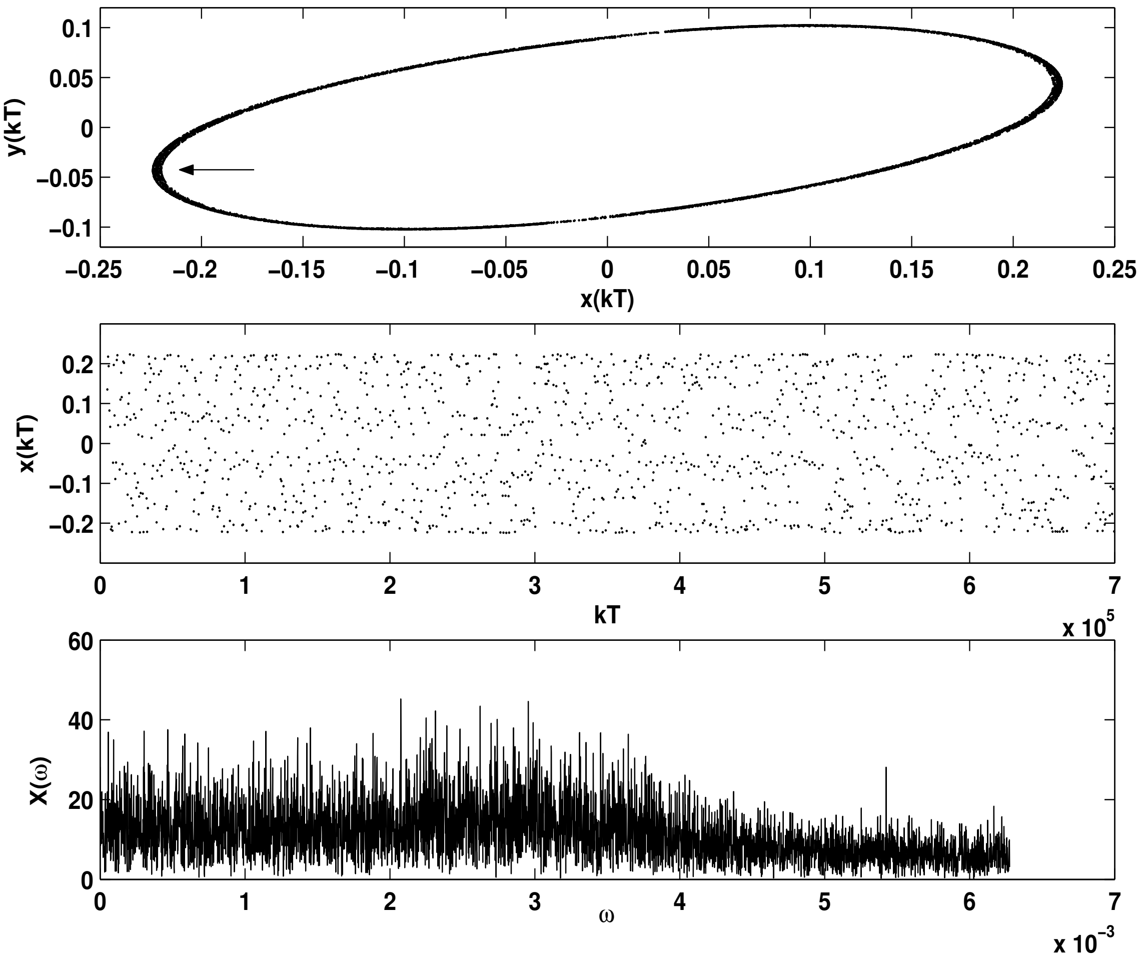

Fig. 13. Strange attractor, $T = 500.5, \varepsilon_1 = 0.52, \varepsilon_2 = \varepsilon_3 = 0$. Time-T map projected onto $x - y$ plane (top), $x(kT)$ versus kT (middle), frequency spectrum of $x(kT)$ (bottom).

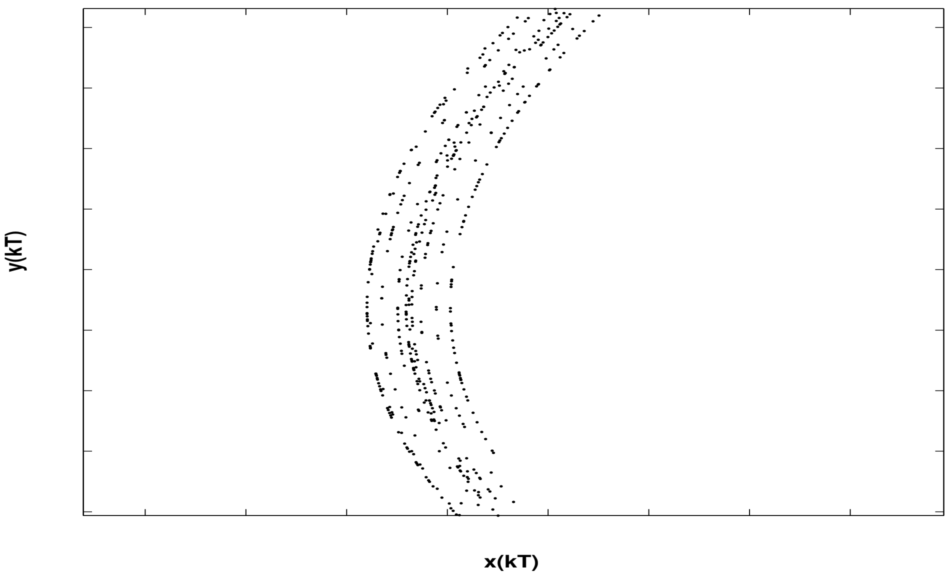

Fig. 14. Magnification of the indicated area of Fig. 13.

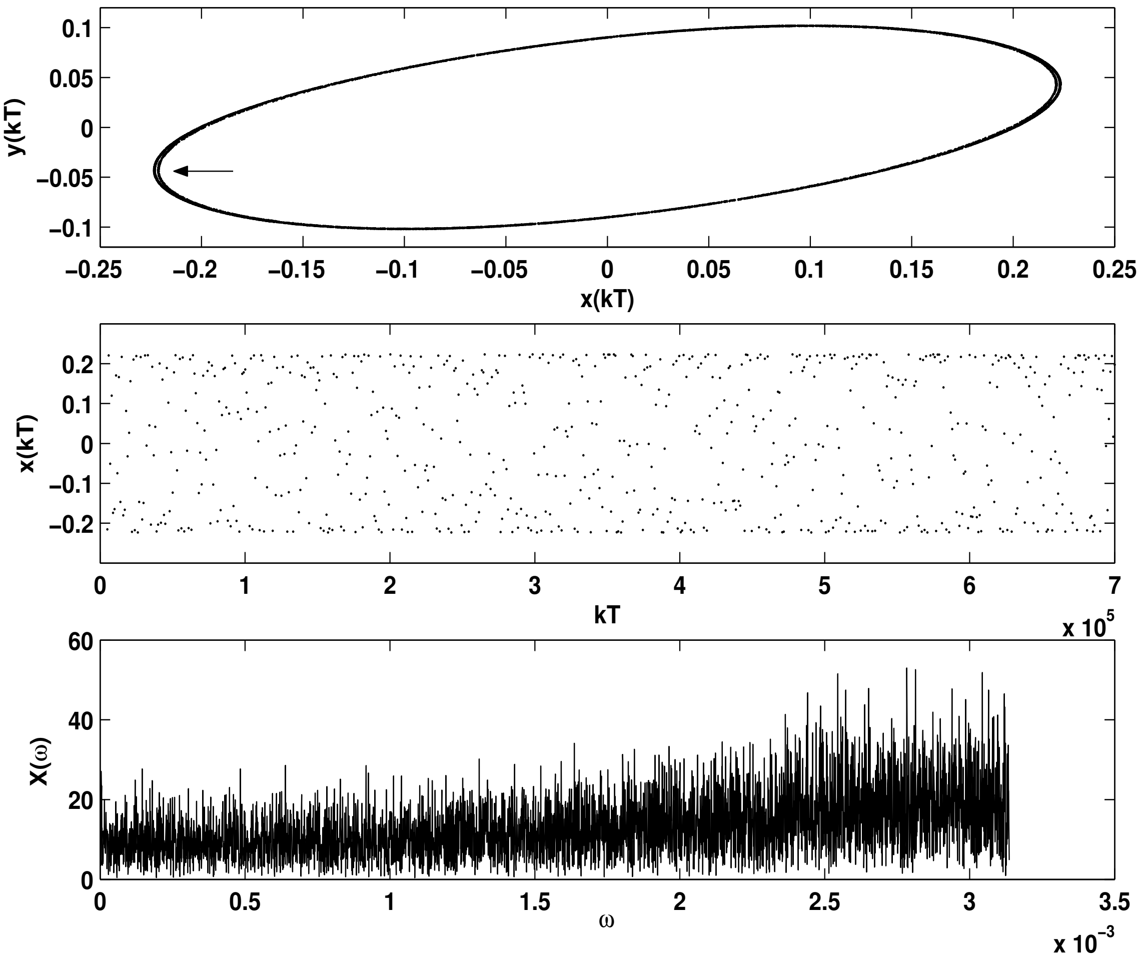

Fig. 15. Strange attractor (Asynchronous case), $T = 1001.5, \varepsilon_1 = 0.52, \varepsilon_2 = 0.32, \varepsilon_3 = 0.26$. Time-T map projected onto $x - y$ plane (top), $x(kT)$ versus kT (middle), frequency spectrum of $x(kT)$ (bottom).

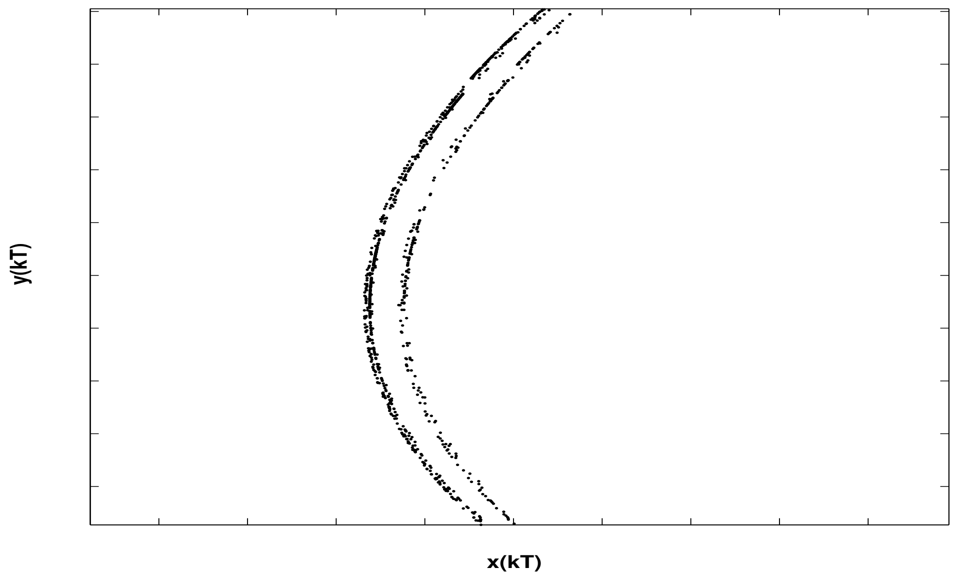

Fig. 16. Magnification of the indicated area of Fig. 15.

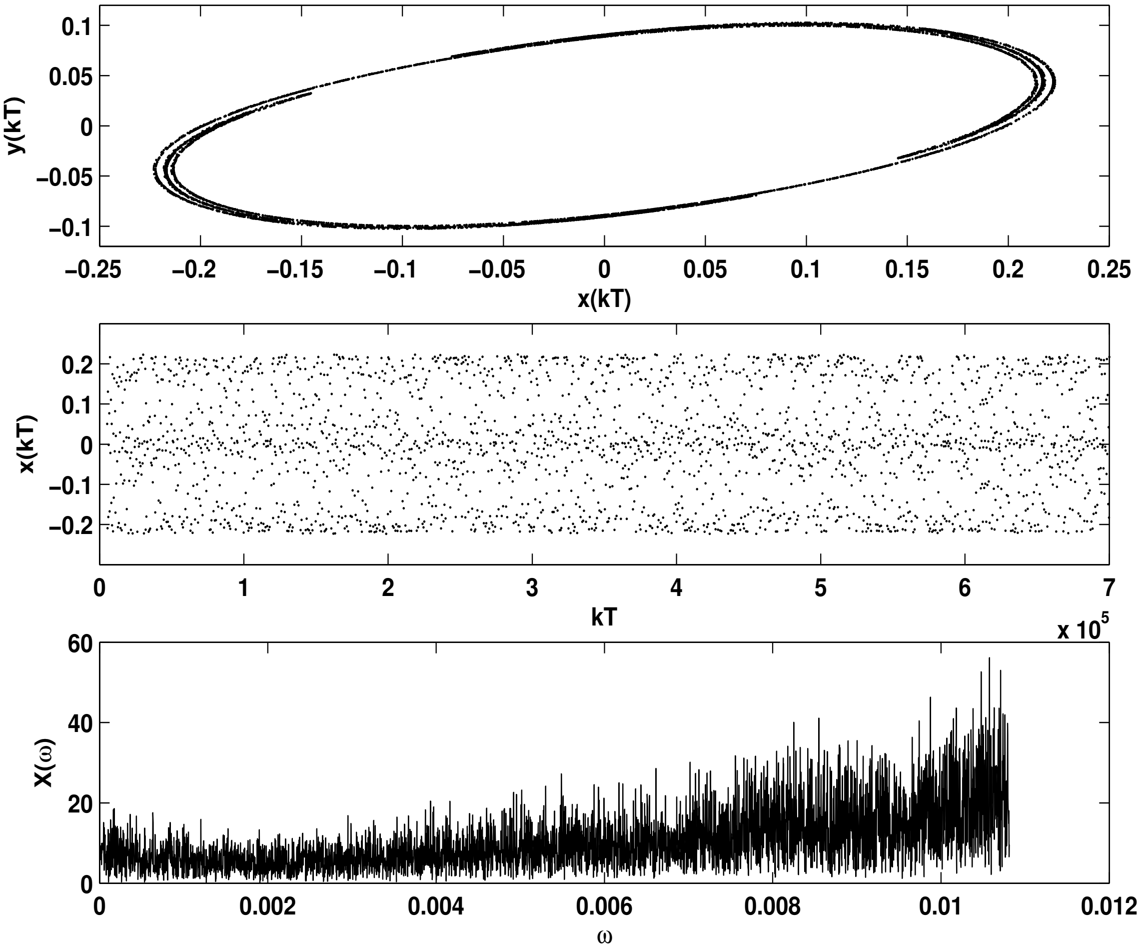

Fig. 17. Strange attractor (Asynchronous case), $T = 290.5, \varepsilon_1 = 0.52, \varepsilon_2 = 0.32, \varepsilon_3 = 0$. Time-T map projected onto $x - y$ plane (top), $x(kT)$ versus kT (middle), frequency spectrum of $x(kT)$ (bottom).

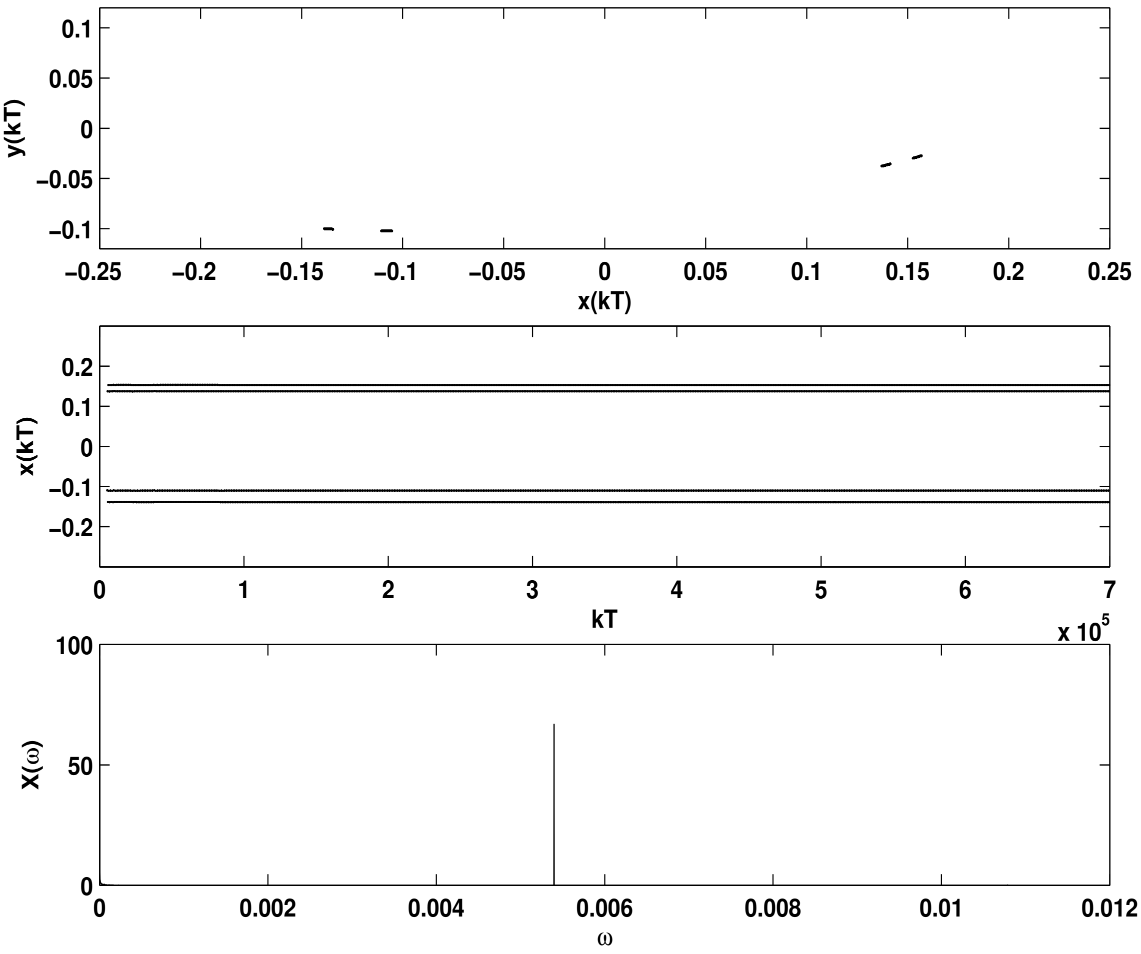

Fig. 18. Periodic Sinks (Asynchronous case), $T = 291, \varepsilon_1 = 0.52, \varepsilon_2 = 0.32, \varepsilon_3 = 0$. Time-T map projected onto $x - y$ plane (top), $x(kT)$ versus kT (middle), frequency spectrum of $x(kT)$ (bottom).

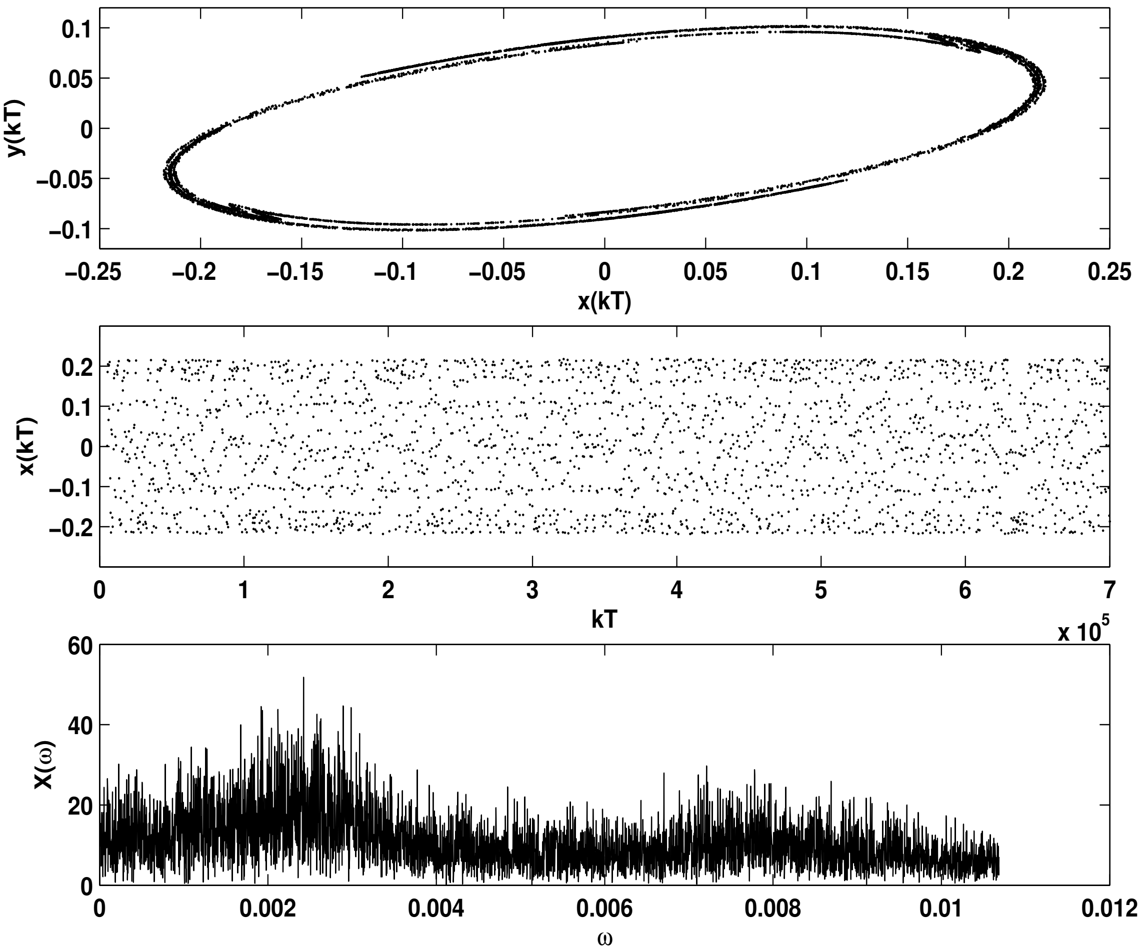

Fig. 19. Strange attractor (Asynchronous case), $T = 294, \varepsilon_1 = 0.52, \varepsilon_2 = 0.32, \varepsilon_3 = 0.26$. Time-T map projected onto $x - y$ plane (top), $x(kT)$ versus kT (middle), frequency spectrum of $x(kT)$ (bottom).

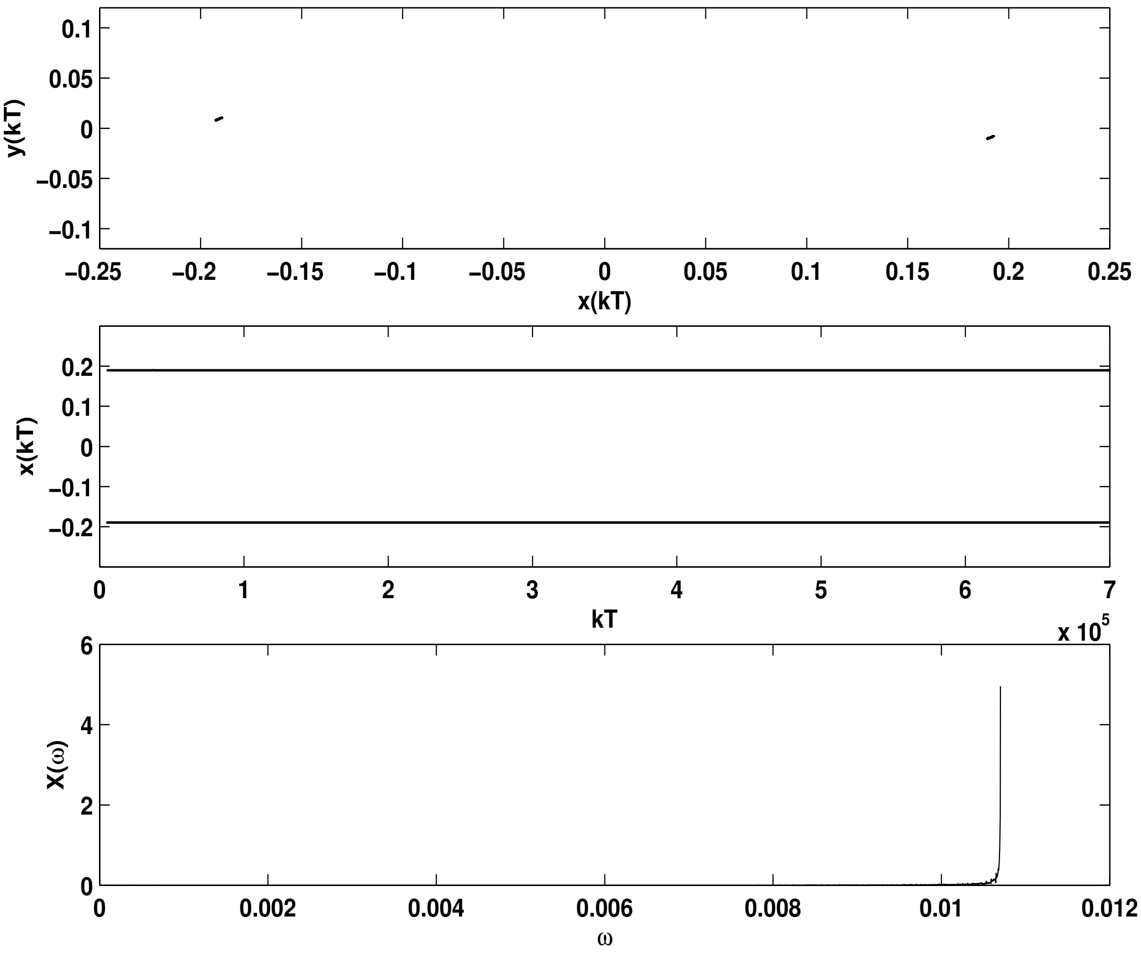

Fig. 20. Periodic Sinks (Asynchronous case), $T = 293.5, \varepsilon_1 = 0.52, \varepsilon_2 = 0.32, \varepsilon_3 = 0.26$. Time-T map projected onto $x - y$ plane (top), $x(kT)$ versus kT (middle), frequency spectrum of $x(kT)$ (bottom).

REFERENCES

[1] M. L. Cartwright and J. E. Littlewood, "On nonlinear differential equations of the second order," *J. London Math. Soc.*, vol. 20, pp. 180–189, Dec. 1945.

[2] N. Levinson, "A second order differential equation with singular solutions," *Ann. Math.*, vol. 50, no. 1, pp. 127–153, 1949.

[3] S. Smale, "Differantiable dynamical systems," *Bull. AMS*, vol. 73, pp. 717–817, 1967.

[4] M. Levi, "Qualitative analysis of periodically forced relaxation oscilations," *Mem. AMS*, vol. 214, pp. 1–147, 1981.

[5] J. Guckenheimer and P. Holmes, *Nonlinear Oscillations , Dynamical Systems and Bifurcations of Vector Fields*, 5th ed., ser. Applied Mathematical Sciences. New York: Springer-Verlag, 1997, p. 155.

[6] M. Jakobson, "Absolutely continues invariant measures for one-parameter families of one-dimensional maps," *Commun. Math. Phys.*, vol. 81, pp. 39–88, 1981.

[7] M. Misiurewicz, "Absolutely continuous invariant measures for certain maps of an interval," *Publ. Math. IHES.*, vol. 53, pp. 17–51, 1981.

[8] T. Nowicki and S. V. Strien, "Absolutely continuous invariant measures under a summability condition," *Invent. Math*, vol. 105, pp. 123–136, 1991.

[9] M. Rychlik, "Another proof of jakobson's theorem and related results," *Ergodic Theory and Dynamical Systems*, vol. 8, pp. 83–109, 1988.

[10] M. Benedicks and L. Carleson, "On iterations of $1 - ax^2$ on $(-1, 1)$," *Ann. Math.*, vol. 122, pp. 1–25, 1985.

[11] ——, "The dynamics of the Hénon map," *Ann. Math.*, vol. 133, pp. 73–169, Nov. 1991.

[12] Q. Wang and L.-S. Young, "Strange attractors with one direction of instability," *Commun. Math. Phys.*, vol. 218, pp. 1–97, Nov. 2001.

[13] ——, "Toward a theory of rank-one attractors," *In preprint*, 2004.

[14] ——, "From invariant curves to strange attractors," *Commun. Math. Phys.*, vol. 225, pp. 275–304, 2002.

[15] ——, "Strange attractors in periodically-kicked limit cycles and Hopf bifurcations," *Commun. Math. Phys.*, vol. 240, pp. 509–529, 2002.

[16] R. N. Madan, *Chua's Circuit: A Paradigm for Chaos*. Singapore: World Scientific, 1993.

[17] L. O. Chua, "Chua's circuit. An overview ten years later," *J. Circuits Syst. Comput.*, vol. 4, pp. 117–159, Apr. 1994.

[18] Q. Wang and A. Oksasoglu, "Strange attractors in periodically kicked Chua's circuit," *Int. J. Bifurc. Chaos*, vol. 16, no. 1, pp. 000–000, 2005.

[19] M. Bernardo, F. Garofalo, L. Glielmo, and F. Vasca, "Switchings, bifurcations, and chaos in DC/DC converters," *IEEE Trans. Circuits Syst. I.*

[20] A. Aroudi, L. benadero, E. Toribio, and G. Olivar, "Hopf bifurcation and chaos from torus breakdown in a PWM voltage-controlled DC-DC Boost converter," *IEEE Trans. Circuits Syst. I.*

[21] T. Saito, "A chaos generator based on quasi-harmonic oscillator," *IEEE Trans. Circuits Syst. I.*

[22] T. Kousaka, T. Ueta, and H. Kawakami, "Bifurcation of switched dynamical systems," *IEEE Trans. Circuits Syst. II.*

[23] K. Mitsubori and T. Saito, "Mutually pulse-coupled chaotic circuits by using dependent switched capacitors," *IEEE Trans. Circuits Syst. I.*

[24] K. Miyachi, H. Nakano, and T. Saito, "Response of a simple dependent switched capacitor circuit to a pulse-train circuit," *IEEE Trans. Circuits Syst. I.*

[25] W. Lin and J. Ruan, "Chaotic dynamics of an integrate-and-fire circuit with periodic pulse-train input," *IEEE Trans. Circuits Syst. I.*

[26] R. Kılıç, "A harmony of linear and nonlinear oscillations: Wien bridge-based mixed-mode chaotic circuit," *J. Circuits Syst. Comput.*, vol. 13, pp. 137–149, 2004.